# Biaxial Testing of Elastomers - Experimental Setup, Measurement and Experimental Optimisation of Specimen's Shape

H. Seibert, T. Scheffer, S. Diebels

*The present article deals with the setup and the control of a biaxial tension test device for characterising the material properties of elastomers. After a short introduction into the experimental setup a brief explanation of the benefits of a biaxial tension test is given. Furthermore the analysis of this test will be discussed. Therefore, the used optical field measurement by digital image correlation for analysing the strains is shortly introduced to the reader. Additionally, the basic concepts of the calculation of an inverse boundary problem for identifying the material's parameters are imposed. However the main focus is laid on the experimental optimisation of the specimen's geometry, whereupon a nearly hyperelastic, incompressible silicone is used to get the experimental results. The resulting geometry will be specially fitted to the requirements of elastomers. The tested geometries and the evaluation of the experiments will be explained as well as the resulting quality factor for the suitability of a specimen's shape. After all, a short validation of the foregoing considerations will be presented.*

## 1  Introduction

The significance of simulations in the construction and development of products steadily increases. The expensive and time-consuming prototype-construction has to be minimised because of increasing demands on the products and simultaneously the enforcement of decreasing the costs of the production process. In order to ensure the functionality of the commodity, reliable tools for simulations like the finite element method have to be made available. Especially elastomers engage a more and more important role in modern product engineering and fulfil a wide range of functional tasks. Typical application ranges are sealings, vibration absorption, acoustic insulation or arbitrary combinations of those, cf. Eyerer et al. (2008); Gent (2001).

With regard to a certain simulation of these materials an adequate material model has to be implemented in the simulation tool. The characteristics of such models vary with the application that has to be examined. In general, the type of the experiment that is used to identify the parameters of the constitutive law is supposed to be as similar as possible to the real practice, though the focus can lie on different specific material effects, e. g. the modelling of the often occurring viscoelasticity as mentioned exemplarily in Haupt and Lion (2002), Lion (2000) or Reese and Govindjee (1998), the modelling of the Payne-effect, cf. Payne (1962), which describes an amplitude-, frequency- and filler-amount-dependent softening effect of cyclically loaded filled elastomers, or the influence of the temperature on the material behaviour, which is typically more significant with polymers than with metals, cf. Rey et al. (2013).

In this context, the impact of multiaxiality is often underestimated in industrial use. The main reason for that wilful neglect is the preeminence of the uniaxial tension test, which represents the most common experiment to obtain material parameters, cf. Brown (2006). The significance of this test method is founded in its comparatively simple execution on the one hand, and in its simple analysis on the other.

The importance of the adaption of an approach to display the material behaviour in a proper way is shown in Koprowski-Theiß et al. (2012). Therein a model for a sealing profile out of the automotive engineering is presented. On purpose to describe the sealing behaviour of the porous elastomer that is treated, the material is tested under hydrostatic pressure which is a more specific form of multiaxial deformation state.

The literature provides many setups for equibiaxial tension tests. An equibiaxial tension test can be realised by a uniaxial pressure test, cf. Chatraei and Macosko (1981), by a bubble inflation test, cf. Baaser and Noll (2009), or by a stretching frame, presented in Detrois (2001) for example.

In case of multiaxial deformations with cyclic loadings as it is common with car tyres for example, one has to arrange dynamic multiaxial tests to examine the material properties of interest. Examples for tests designed for this special demands are shown by Freund et al. (2011), Gent (1960) or Ihlemann (2002); Klauke et al. (2010).
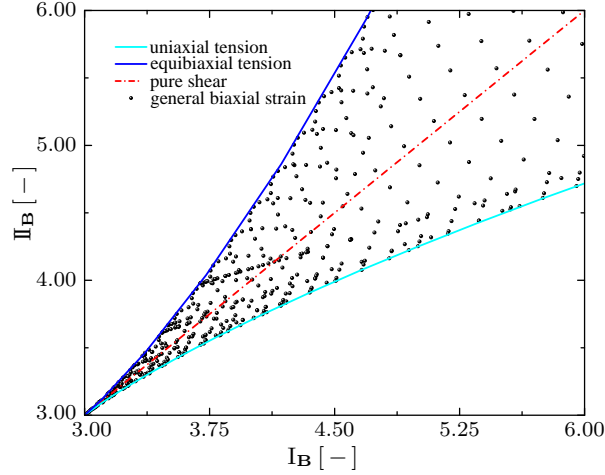
Figure 1: plane of invariants according to Treloar (1975). Possible deformation states are limited to the range between uniaxial tension and equibiaxial tension

To explain the need of multiaxial material models the plane of invariants according to Treloar (1975) is consulted. Therein, all possible deformation states of a structure can be recognised, provided that the material is incompressible which is sufficiently fulfilled with the considered silicone rubber and many other elastomers. Basically, that plane is spanned by the first and the second principal invariants of the left Cauchy-Green deformation tensor $\mathbf{B}$, cf. Baaser and Noll (2009); Johlitz and Diebels (2011); Treloar (1975). These principal invariants are given by

$$
\begin{aligned}
\mathrm{I_B} &= \mathrm{tr}\mathbf{B} = \mathbf{B} : \mathbf{I} \\
\mathrm{II_B} &= \frac{1}{2}\left[(\mathbf{B} : \mathbf{I})^2 - \mathbf{B}^T : \mathbf{B}\right] \\
\mathrm{III_B} &= \det \mathbf{B} = 1.
\end{aligned}
\tag{1}
$$

Taking into account the material's incompressibility, the third principal invariant is equal to one, which is equivalent to the volume conservation.

Applying the numerical values for uniaxial tension, equibiaxial tension, cf. Baaser and Noll (2009); Baaser et al. (2011); Chevalier and Marco (2002); Sasso et al. (2008) and pure shear, one gets the limitations of possible deformation states between the curve of equibiaxial tension and uniaxial tension. All achievable deformations are within these curves, cf. Fig. 1.

 Hence, a uniaxial tensile test is represented by the lower limitation curve in Fig. 1, pursuant to that, an equibiaxial tension test by the upper curve. Every other state of deformation is located between these curves. These arbitrary states cannot be considered if models are used that are calibrated by uniaxial tension tests only. The reason is found in the given ratio of the first and the second principal invariant during the uniaxial test.

If the real application is conform to the executed experimental setup, this approach provides acceptable results. Considering the deformation of a typical part in automotive engineering, the problems are obvious. Fig. 2a) shows a CAD-reproduction of a typical engine mount of a car. It consists of a two-piece supporting frame made of steel, connected with two elastomer buffers. In the static case only the weight of the engine loads the bearing, which is in accordance with a uniaxial loading situation, cf. Fig. 2b). But the complexity of the assembly leads to a deformation field, which is different from a uniaxial tension or pressure. This is pointed out in Fig. 2c), where the deformations of the buffers, in detail the combinations of the first and second principal invariants of $\mathbf{B}$, are logged pointwise. The simulation is computed with Comsol Multiphysics®. One has to notice that Fig. 2c) overestimates the deformation for better understanding. The fact that the position of a deformation state within the plane of invariants plays an important role for the material behaviour was already shown by Rivlin and Saunders (1951) or by Treloar (1976). Following these results, Johlitz and Diebels (2011) developed an experimental setup, which allows to reach arbitrary admissible points in the plane of invariants. The ideas presented in Johlitz and Diebels (2011) will be refined and extended in the present article. Especially the experimental optimisation of the specimen's shape will provide the main focus.
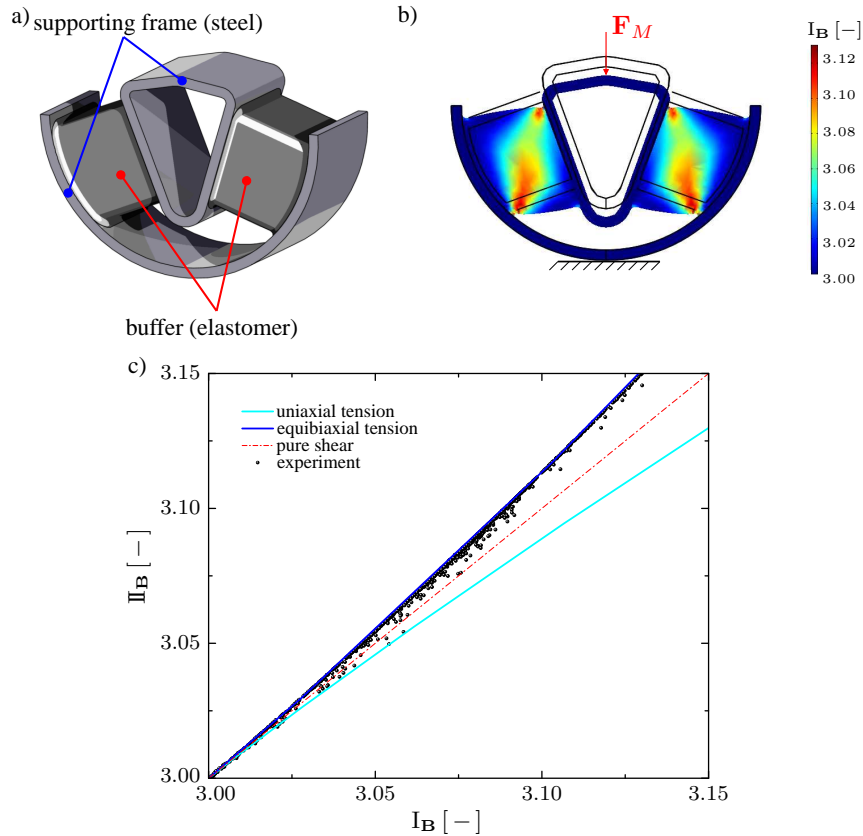
Figure 2: Example part engine mount: a) CAD-reproduction; b) FE-simulation; c) plane of invariants with deformed states according to the simulation

## 2 The Testing Device

The used biaxial testing device is based on the setup described in Johlitz and Diebels (2011). It consists of a specially built frame fitted with four stepper motors associated with spindle units, cf. Fig. 3. Two of each linear drives are aggregated to an axis, whereas the two axes are ordered crosswise. By the transmission to the spindle unit there are four linear slides. The opposite engines move synchronously but counter-rotating, which has several advantages. On the one hand the centre of a specimen that is clamped in the middle between the two linear slides doesn't leave its position although the slides erase from each other. On the other hand, the arrangement doubles the testing velocity compared with the velocity of each slide.

It is possible to control both axes independently of each other, and in this way the possibility is given to reach any admissible point in the plane of invariants. Allowing a suitable trajectory in the invariant plane during an experiment it is possible to generate a data pool for determining the material behaviour at any deformation state.

The corresponding reaction forces are measured by two S-shaped force sensors, one in each axis. The complete setup of the device and a detailed view on the clamped specimen are given in Fig. 3.

### 2.1 Control

Due to the fact that the device is an in-house development, the deposited coding of the machine can be adapted individually to the demanded deformation profile. In the following section, the basics of the programming are exposed more detailed.

As coding environment the software LabView® by National Instruments® comes into operation. With respect to the peculiar requirements in terms of synchronisation of the corresponding axes, a real-time system was chosen to execute the controlling tasks. As hardware components the CompactRIO®-Controller with convenient cSeries-Modules®, also by National Instruments®, are used. By the choice of that real-time environment, a special coding architecture has to be followed.

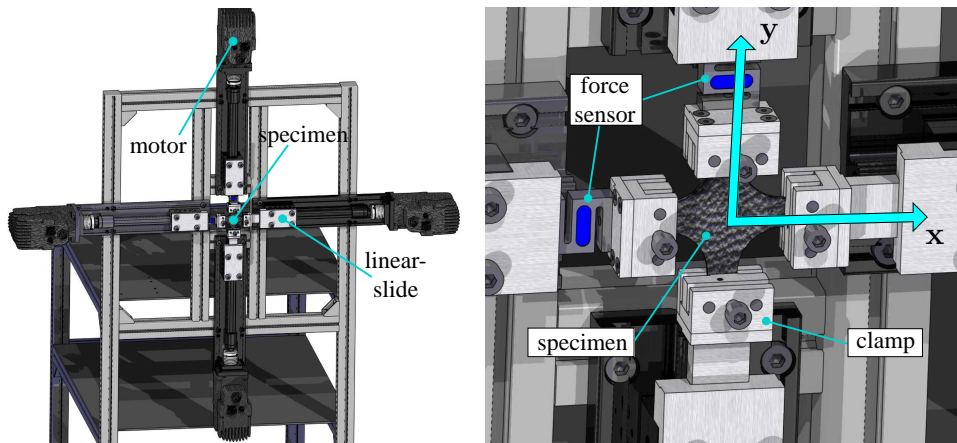LabView®-RealTime programmings consist of a three part program structure on different hardware modules:

Figure 3: testing device, left: complete setup; right: detailed view on specimen

- FPGA (field programmable gate array)
  The FPGA integrated in the cRIO-Controller is the fastest system-component, which comes up to a hard-wired digital circuit in its clock frequency. In this chip all communication tasks are executed which are the reading-in of the sensor signals, the writing-out of the machine instructions and also the reading-in of the current angularity of the motors. The last permits to calculate the current slide position by using the spindle slope.

- cRIO-Controller
  The cRIO-Controller is the second hardware-component which is used. It is also built for real-time applications and operates as an interface between the experimenter and the machine. The main aspects of its programming are data processings, in detail scaling of input-signals or the preparation of control commands. Besides simple single commands the virtual instrument provides the possibility to send out a sequence of commands, which is generated by a separate application, the so called sequence editor. Test methods generated by this sequence editor can be modified and repeated any number of times, so the experimental effort is minimised.

- Host PC
  The next discussed software component is not necessary for the handling of the system but for data-logging. This control-part of the device works on a customary computer and has the task to file the upcoming measurements or images for the optical strain measurement.

Additionally to traditional commands for the run-up to a specified slide-position, the experimenter is able to schedule more complex sequential arrangements. The creation of such a sequence leads to automated test procedures which can be iterated at the push of a button. There are several basic modules the sequences can be constructed with, including linear positioning with defined velocity, stepwise loading of the specimen with holding-times or cyclic tests with moderate frequencies. Furthermore data operations like logging the measured signals with certain sampling rates to reduce the data overhead at long term but fast cycling tests and taking and storing photos at defined times.

Moreover it has to be mentioned that both axes can be moved independently from each other. This ensures that a desired path through the plane of invariants, as displayed in Fig. 7, can be performed. The innovation compared to Johlitz and Diebels (2011) is rooted in the automated execution of the sequences. Originally, the commands had to be initiated by the experimenter, having its disadvantages in matters of reproducibility and effort of time on the part of the operator.

In detail, the proposed testing guidance is given by several segments. At first, the $x$-axis is prestretched to a defined position. This yields a nearly uniaxial deformation in the stretched axis which correlates in a starting point on the lower limiting curve in the plane of invariants. By holding the $x$-axis at the given position and stepwise stretching of the $y$-axis, the deformation in the centre of the specimen leaves more and more the uniaxial state. If the deformation is equal in both directions, the upper limiting curve is reached being identical with an equibiaxial deformation state. Further stretching in $y$-direction results in a further removal from that curve. By repeating the tests for different prestretches of the $x$-axis, curves as plotted in Fig. 7 result in the course of the experiments. There has to be mentioned, that Fig. 7 only displays three curves as an example. Lower and higher values can be set by an appropriate choice of the prestretching in $x$-direction.

## 2.2 Optical Strain Measurement

In this section, the basics of optical strain measurement are introduced. Furthermore, the differences between the spatial discretised acquisition as proposed in Johlitz and Diebels (2011); Koprowski-Theiß et al. (2011) and the continuous measurement as used in this article, are demonstrated, see also Avril et al. (2008); De Crevoisier et al. (2012). The resulting consequences for the development of a material model are shown. The goal of the following paragraphs is to generate a fundamental appreciation for the presented methods. For more details concerning the particular techniques the reader is referred to pertinent literature, e. g. Chu et al. (1985); Pan et al. (2009); Schmidt et al. (2003a,b); Sutton et al. (2000, 2009); Yaofeng and Pang (2007).

### 2.2.1 Strain Measurement by Edge-Detection

Initially, the relatively simple variant of strain measurement by edge-detection is suggested. Although the results depicted later on are not obtained by this method, the relevance of the measuring-procedure for the design of the specimen's shape has to be distinguished. Meanwhile the method of edge-detection for determining strains is commonly used. It is predicated on the assumption, that the strain of a discrete increment of the specimen is representative for the strain over the whole sample, i. e. the strain field has to be homogeneous. A typical field of application is the uniaxial tension test on condition that uniform stretches occur. Usually in this case, the specimen's surface is marked by paint with a quadratic field. Therefore, the coating has to exhibit a high contrast towards the surface of the sample.

During the experiment, the marked field has to be captured by a camera, which is adapted to the device. In this context, the advantage of the stationarity of the specimen's centre is obvious, because of the missing necessity of tracking the mark.

The taken photos have to be interpreted by an image processing software afterwards. In this software, the extension of the put up mark has to be detected, whereby the high contrast between mark and surface of the specimen guarantees the reliable reconnaissance of the edges, which is essential for an automated interpretation. The identified dimensions in each direction, cf. Fig. 4, can be used to calculate the strain corresponding to

$$\lambda_1 = \frac{l}{l_0}, \qquad\qquad \lambda_2 = \frac{w}{w_0} \qquad\qquad (2)$$

with

$$\lambda_i = 1 + \varepsilon_i.$$

Therein, $l$ stands for the length of the mark and $w$ for its width. The index $(\cdot)_0$ characterises the reference state. Since the strain is a dimensionless quantity the measurement of $l$, $l_0$, $w$ and $w_0$ can be in pixels. The strain of the discrete increment is given by the comparison between the current dimensions and those in the reference state. For the special case of a uniaxial tension test with homogeneous sample material the measured strain is conform with the strains all over the uniform area of the specimen, assuming that the discrete increment is sufficiently far from the clamps.

The limits of the presented method are revealed by its derivation. First of all, Eqn. (2) expects geometrically linear behaviour, which causes errors that are not negligible for large deformations. Furthermore, the range of validity is limited to homogeneous materials on the one hand and uniform deformations on the other. Inhomogeneous materials have a disposition to necking, with the consequence that the area of maximum strain is located to one point and can be simply overlooked. This problem can occur even with a very uniform specimen as given in DIN EN ISO 527-2 (dogbone-shaped). In conjunction with more complex geometries the boundaries of this treatment are nearly reached.

### 2.2.2 Optical Field Measurement by DIC

In this article, the applied strain measurement method is an optical procedure based on digital image correlation (DIC) algorithms.

The used commercial tool is the software Vic2D®, developed by Correlated Solutions®, cf. Correlated Solutions (2010). Therein, the recognition of random speckle patterns which are allowed to move arbitrarily through the
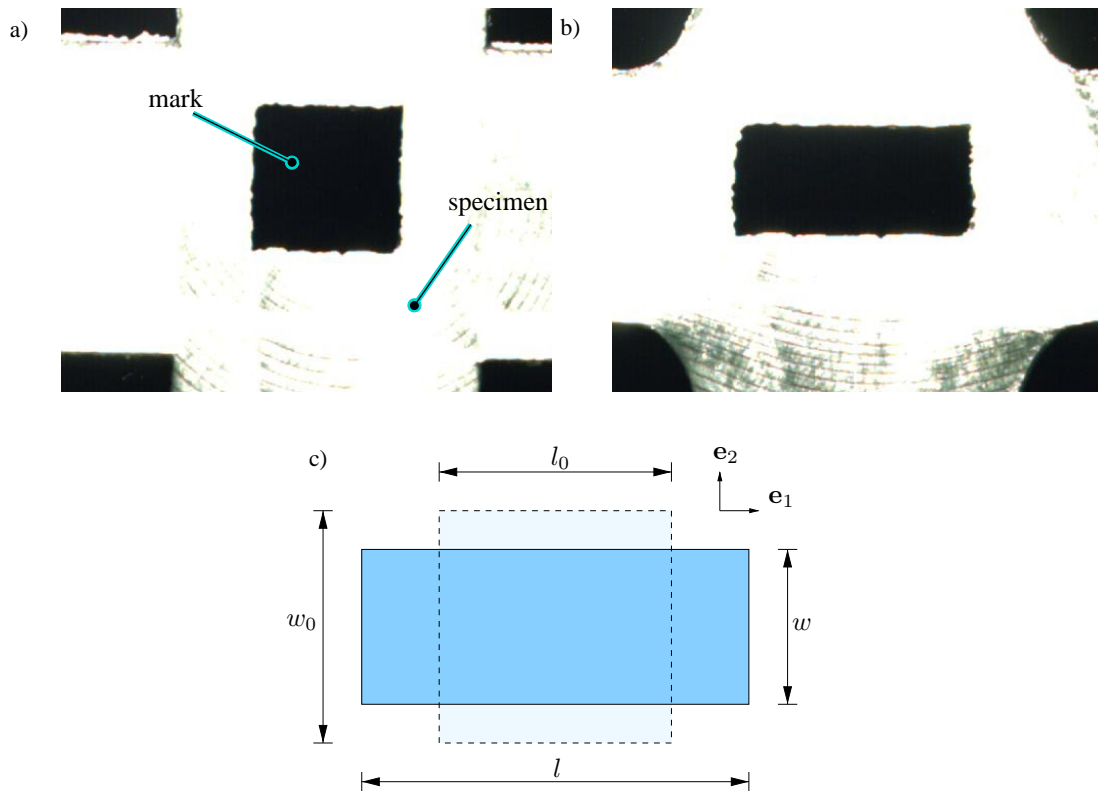
Figure 4: strain measurement with edge-detection: a) reference state; b) deformed state; c) interpretation

captured image plane, is implemented. On the one hand, the fluctuation of discrete image details over a series of images is traced, on the other hand, the deformation of that special detail is detected by the observation of similarities. Fig. 5 displays the basic functional principles, Correlated Solutions (2010). Therein, three distinct configurations are shown, from the left to the right the reference shape with the undeformed quadratic image detail and two further deformed configurations. The marked field of view undergoes a translation and in addition a distortion. By the use of mathematical algorithms like displayed in Sutton et al. (2009), a projection of the actual arrangement onto the reference can be applied. Hence the variation of the specified field of interest can be distinguished. For this procedure it is essential to coat the specimen with an appropriate pattern. It is required that the observed area of the pattern is unique and stochastic, otherwise a reliable recognition is not executable. Regular, oriented structures like rectangles or periodically appearing lines do not match these assumptions which causes inaccuracy in the interpretation. The most simple way to obtain a pattern that fulfils all demands is to produce a random set of points on the surface.

Depending on the type of application various methods of coating specimens have established. Exemplarily there can be mentioned:
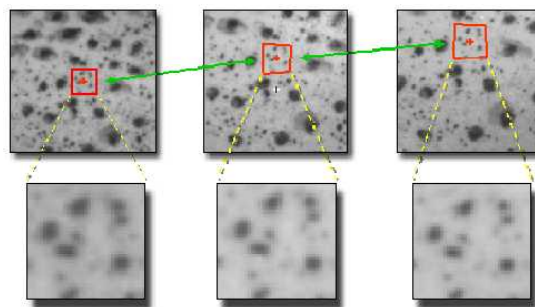


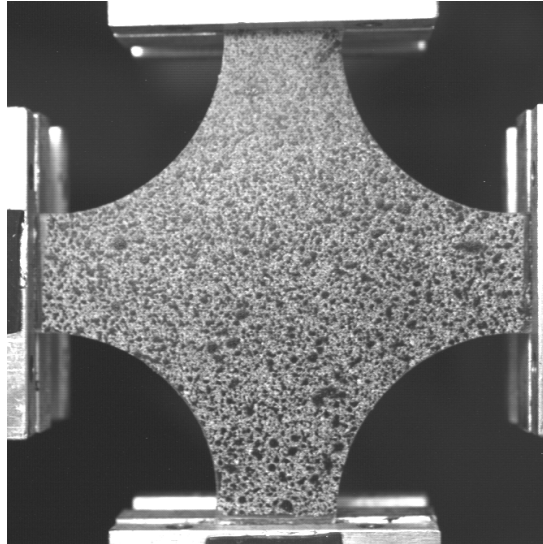Figure 5: functionality of DIC, Correlated Solutions (2010)

Figure 6: speckle-pattern on clamped specimen (type D according to Fig. 10)

- contact lithography,

- charging with toner powder, which is fixed by heating up,

- spray coating.

By combination of the materials to test and the arising costs spray coating is preferred in this case, but transparency of the observed silicone rubber causes further problems. Being aspired to finite deformations the discrete pattern-areas are underlying large translations in the image plane, whereby the necessity of preferably constant lighting conditions over wide ranges increase. Already weak contrasts in the patterns by default can still decrease by irregular lighting conditions, which prohibits the proper execution of DIC-algorithms. According to that, high contrasts have to be ensured a priori. For this reason a smooth, white base coat is applied to the surface before the deposition of the black speckle pattern. Fig. 6 shows a prepared specimen installed in the testing device.

The advantages of the optical field measurement are obvious. The variability of the observed shapes and also the variability of the observed materials make this method a very general type of measuring strains. Furthermore the results are based on finite deformations whereby a linearisation from the beginning can be omitted.
In the presented version of Vic2D® only in-plane deformations can be detected. By the use of a stereoscopic camera system in connection with the extension Vic3D® by the same producer, three dimensional deformations can be observed also, which makes the method still more capable.

## 3   Modelling and Parameter Identification

This section is intended to recapitulate the interpretation of the investigations presented by Johlitz and Diebels (2011). For this purpose only a short overview of the basic concepts pertaining to the proposed material model is given, as the main focus is set on the experimental optimisation of the specimen's shape.
Johlitz and Diebels (2011) have executed uni- and biaxial tension tests with the used silicone rubber ELASTOSIL® RT 625, produced by Wacker Chemie GmbH. The benefit of this material is rooted in the slightly pronounced rate dependency of its strain-stress-relation which leads to very short relaxation times and therewith to a nearly hyperelastic material response. By the works of Johlitz and Diebels (2011) and Chen et al. (2013) isotropy and quasi-incompressibility of this rubber were proved.
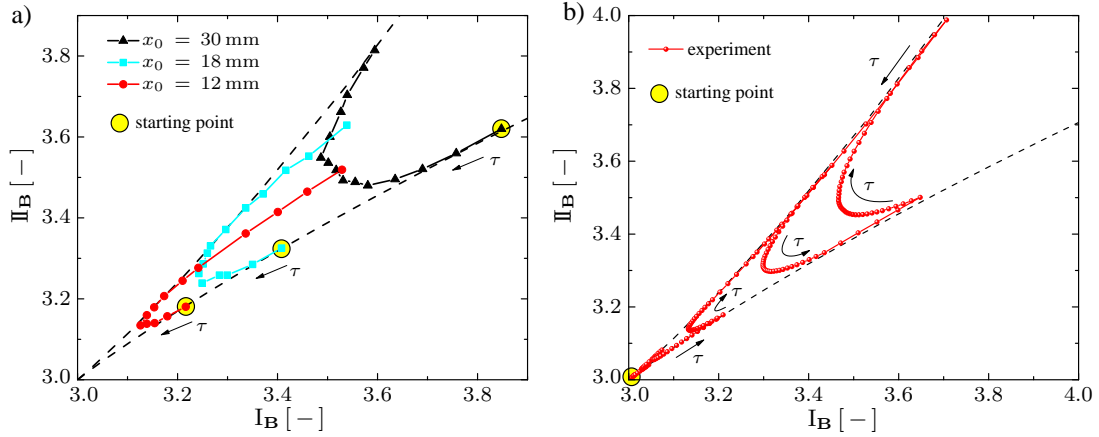
Figure 7: paths in the plane of invariants depending on pre-deformation in $x$-direction: a) experiments by Johlitz & Diebels Johlitz and Diebels (2011); b) current experiment by the use of DIC (sample type D)

### 3.1 Material Modelling

The introducing paragraph points out the importance of the influence of multiaxial deformations on the material behaviour. This section will give an experimental accentuation of this statement by comparing two identified models which were on the one hand identified by uniaxial tension tests and on the other hand by biaxial tension tests. Details concerning the theoretical background can be found in Johlitz and Diebels (2011). Therein, a constitutive law in the form of Eqn. (3)

$$\mathbf{T} = -p\mathbf{I} + 2\rho_0 \frac{\partial \Psi}{\partial \mathrm{I_B}} \mathbf{B} - 2\rho_0 \frac{\partial \Psi}{\partial \mathrm{II_B}} \mathbf{B}^{-1} \tag{3}$$

is proposed, with the Cauchy stress tensor $\mathbf{T}$, the left Cauchy-Green deformation tensor $\mathbf{B}$ as a process variable and the free energy function $\Psi(\mathrm{I_B}, \mathrm{II_B})$ depending on the first and second principal invariant of $\mathbf{B}$. The Lagrangian parameter $p$ is determined by the additional condition of incompressibility. By the dependency on the two principal invariants the model is able to describe deformation states beyond the lower limit curve of uniaxial tension. A commonly used approach is given by a Mooney-Rivlin-model, cf. Mooney (1940). It can be specified as

$$\rho_0 \Psi = c_{10} \left( \mathrm{I_B} - 3 \right) + c_{01} \left( \mathrm{II_B} - 3 \right). \tag{4}$$

In this approach the density $\rho_0$ cancels just in combination with (3) out and the material parameters $c_{10}$ and $c_{01}$ have to be identified.

### 3.2 Parameter Identification

For the identification of the parameters in the Mooney-Rivlin-approach (4) there are two different experiments used in Johlitz and Diebels (2011). The first one is a conventional uniaxial tension test with specimens according to DIN EN ISO 527-2, the second one is a biaxial tension test, executed at specimens of the shape displayed in Fig. 10a). For details about the procedure of the uniaxial experiment, the reader is referred to Johlitz and Diebels (2011); Koprowski-Theiß et al. (2011).

As explained in a former section, the biaxial test consists of a prestretching in $x$-direction and afterwards a stepwise stretching in $y$-direction while holding the $x$-axis constant. After the evaluation of the marked rectangle in the centre of the specimen, a path in the plane of invariants is performed for a certain pre-deformation in the $x$-direction as illustrated in Fig 7a) or b), respectively. At this point one has to notice that the process of identification deviates from the usual procedure. Due to the fact that the region of interest, the biaxially deformed state is located in the centre of the specimen whereas the reaction force is measured at the end of the specimen's arms. Hence it is necessary to identify the two parameters by solving a complete boundary problem with the reaction force as boundary condition and the strains in the measured area as command variable. So the interpretation is carried out by an inverse computation in an adequate simulation tool, e. g., with Comsol Multiphysics® in this case. In a second software the deformation of the centre field calculated in the simulation has to be compared to the deformation optically measured in the experiment. This comparison is calculated by Matlab® and uses the internal

Table 1: resulting model parameters of two experiments

| parameter | uniaxial tension | biaxial tension |
|---|---|---|
| $c_{10}$ [MPa] | 0.151 | 0.111 |
| $c_{01}$ [MPa] | 0.000 | 0.039 |

Optimisation Toolbox®, which generates a new set of parameters. This set of parameters is committed to Comsol Multiphysics® again and a new comparison is started until the difference between the computed and the measured strain becomes minimal.

### 3.3 Results

By the adaptation of the suggested constitutive law to the experimental data and a subsequent simulation of the particular test in Comsol Multiphysics® it is evident, that the model is able to reproduce both corresponding experiments, cf. Fig. 8 a) and b).

The resulting parameters $c_{10}$ and $c_{01}$ of the Mooney-Rivlin approach are mapped in Table 1. On the basis of the numerical value of $c_{01}$ in that table one can recognise the main problem of the uniaxial test. The parameter $c_{01}$ which affects the second principal invariant in the constitutive law, is identified to zero, whereby the Mooney-Rivlin approach is transferred to an approach of Neo-Hookean type. According to that, the resulting material law is able to reproduce uniaxial deformation states only. The fixed ratio between the first and the second principal invariant of **B** in the uniaxial tension test creates the necessity of a further experiment in order to activate the influence of the second principal invariant. By the use of a biaxial tension test it is possible to combine the results of different experiments in one test.

To demonstrate the influence of this inaccuracy, Fig. 8c) and d) show a crosswise simulation. The uniaxial tension test is simulated with the model obtained by interpretation of the biaxial test in Fig. 8c), the contrary case, thus the simulation of the biaxial experiment under utilisation of the uniaxially generated model is shown in Fig. 8d). For better understanding in the case of the biaxial experiments, they are plotted in the form stretch on the $y$-axis and a dimensionless loading parameter $\tau$ on the $x$-axis. This parameter $\tau$ is calculated by the ratio of the experimental time and the duration of the test. Inside these figures $(\cdot)^{UA}$ stands for the model adapted to the uniaxial data and $(\cdot)^{BA}$ adapted to the biaxial test.

Concluding one can see that the uniaxially performed model doesn't reproduce the biaxial test, i. e. the deviation between measured and simulated data increases with increasing load, otherwise, the biaxially performed model reproduces the uniaxial data well, at least in a certain area, cf. Fig. 8c) and d). The difference between the simulation of the biaxially calibrated model and the uniaxial experiment can be explained by means of Fig. 7b). Prestretching one axis while holding the other constant does not produce a perfectly uniaxial deformation state. Clamping of the perpendicular axis causes a deformation state which is slightly different from the uniaxial curve. Furthermore the biaxially calibrated model is performed by a maximum stretch $\lambda_i^{max} \leq 1.4$ at the displayed experiment, cf. Fig. 8b). Significant deviations between the uniaxially and biaxially calibrated models in Fig. 8c) occur at stretches higher than $\lambda_i^{max}$ which is the extrapolating area of the biaxial model. By the execution of biaxial experiments with higher maximum strains the biaxial model leads to a better quality than the uniaxial one.

With these results it can be established, that the choice of a suitable constitutive law in combination with a biaxial tension test can lead to the ability to predict a material behaviour under complex deformations as they are commonly given in reality, cf. Fig. 2. Models identified by the use of uniaxial tests often fail in this application.

### 4 Experimental Optimisation of Specimen's Shape

Basically, the applicability of the proposed method was proved in Johlitz and Diebels (2011). Certainly, enhancements can be applied by modifying some details. One possible upgrade is the optimisation of the used specimen's geometry, which provides the main focus of this article. Relating to this topic, several articles can be referred to, though the construction of the specimen's geometry strongly depends on exterior requirements, like the type of the observed material with the applicable manufacturing techniques. Hence, constraints are built by producibility of the specimens or the chosen method of measuring, e. g. strain measurement by optical field measurement or edge detection.
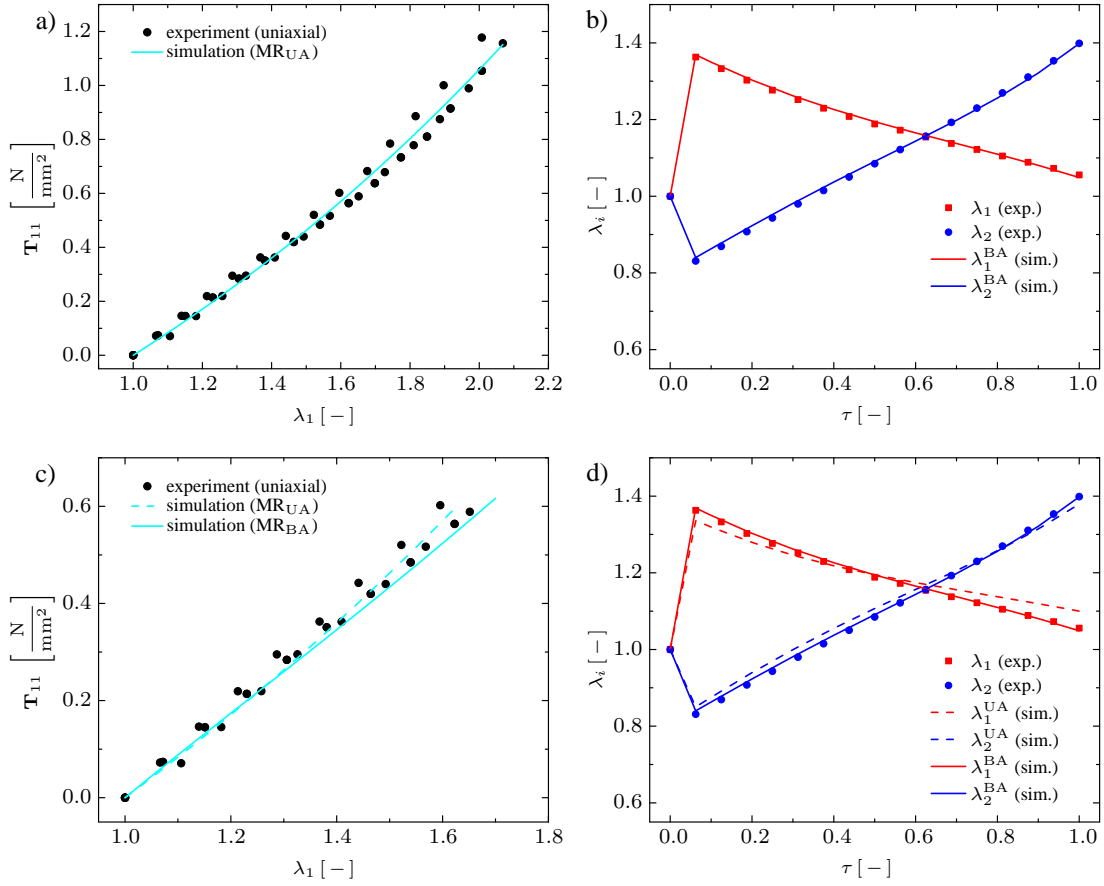
Figure 8: adaptation of measured data: a) fit uniaxial exp.; b) fit biaxial exp.; c) uniaxial and biaxial fit - uniaxial exp.; d) uniaxial and biaxial fit - biaxial exp.

In the present case, elastomers are mainly tested, whereby restrictions concerning the machining of raw materials are given. Chipping technologies for example are only useful in rare cases. Furthermore, it is reasonable to extract the specimens out of the running production to guarantee the equality between the specimen's material behaviour and that of the real component. Cutting the specimen out of a typical geometry like a membrane without the necessity of an aftertreatment, is very convenient.

Overviews over investigations of geometries for biaxial testing, which were executed so far, are given by Ohtake et al. (1998) or Kuwabara (2007). In the course of these, general principles of shaping the specimens as well as actual characteristics of them are illustrated.

In the scope of small deformations, commonly occurring with metals or carbon fibres, Makinde et al. (1992), Tiernan and Hannon (2012) or Demmerle and Boehler (1993) can be named. For investigations of large multiaxial deformations one can name Promma et al. (2009) or Silberstein et al. (2011).

A very similar testing device to the proposed one here is given by Kahraman and Haberstroh (2013). Nevertheless there are significant differences in the design of the specimen's shape. This aspect will be picked up later in this article.

In a first step in the optimisation of the samples' geometry, the requirements have to be scheduled. By the use of optical field measurement, the demands on the geometry with regard to its homogeneity are weakened, because of the availability of the test piece's deformation in every section. Although there has to be simulated the full inverse problem due to the absence of an analytical solution.

Therefore, the goal of the investigations can be defined as follows: Find the shape of a specimen leading to a biaxially deformed area with maximum range and, in addition, high strains in the region of interest. Moreover, the constraints on the material outside this biaxial area have to be as small as possible, which means a kind of overall-homogeneity. With respect to manufacturing the samples, the raw material was predefined as a membrane without the need of changing the specimen in thickness-direction.

## 4.1 Tested Geometries

Based on the sample geometry proposed in Johlitz and Diebels (2011), cf. Fig. 10a), six further shapes were created. In order to get information about the dependencies between properties of the samples and their suitability for getting proper results in a biaxial tension test, there are only small variations among the various test pieces. Fig. 10 displays four intermediary stages beginning at the reference geometry in Fig. 10a) up to the finally chosen shape in Fig. 10d). By reasons of clearness, at this point it is relinquished to describe all the geometries in all details but rather a representative choice. Besides the above-mentioned constant thickness of the sample as well
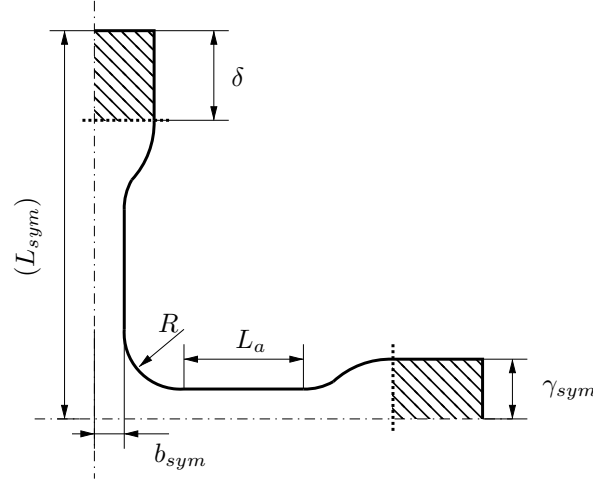


Figure 9: varied parameters for the sample geometry

as their symmetric structure are presupposed. For better understanding, the essential geometrical properties are defined. The centre of the specimen is called crossroad area below. The radius that compounds two perpendicular arms is labelled crossing radius $R$. The arms of the specimen are the ranges parallel to the particular centre line, reaching from the crossing radius to the point with changing cross-section for the clamps.

As illustrated in Fig. 9 the varied parameters are the crossing radius $R$, the width of the arms $b = 2 b_{sym}$ and the length of the arms $L_a$. The region for the clamping jaws has to be a rectangle of the width $\gamma = 2 \gamma_{sym} = 12.5 \, \text{mm}$ and the length $\delta \geq 8.5 \, \text{mm}$. The overall length of the sample $L_s = 2 L_{sym}$ results from the choice of the foregoing parameters.

## 4.2 Quality Criterion

In order to establish a criterion for the grade of biaxiality further deliberations have to be made. In his article, Baaser et al. (2012) proposes a method to describe the deformations in a structure based on modified invariants. The proposed pair of variables allows statements about the intensity of a deformation state and its comparability with another. However, these variables are introduced with intent to create a constitutive law for the particular material.

In the present work, there is the need of such a formulation with regard to describe the intensity of a biaxial deformation state. So the general localisation inside the plane of invariants can be reduced to an equibiaxial state as a special case. Hence, the mathematical formulation of the grade of biaxiality can be transformed into a simple comparison between the strains in both directions.

### 4.2.1 Grade of Biaxiality

This section deals with the introduction of criteria for the grade of biaxiality and also an appropriate regulation for its experimental determination. As mentioned in the paragraph above, one can use the equibiaxial deformation in the crossroad section and compare the resulting strains. After that, a mathematical test function can be created. The results of that formulation can be transferred onto a general biaxial deformation state.

For the following considerations the equality between the coordinate systems of the testing device as illustrated in
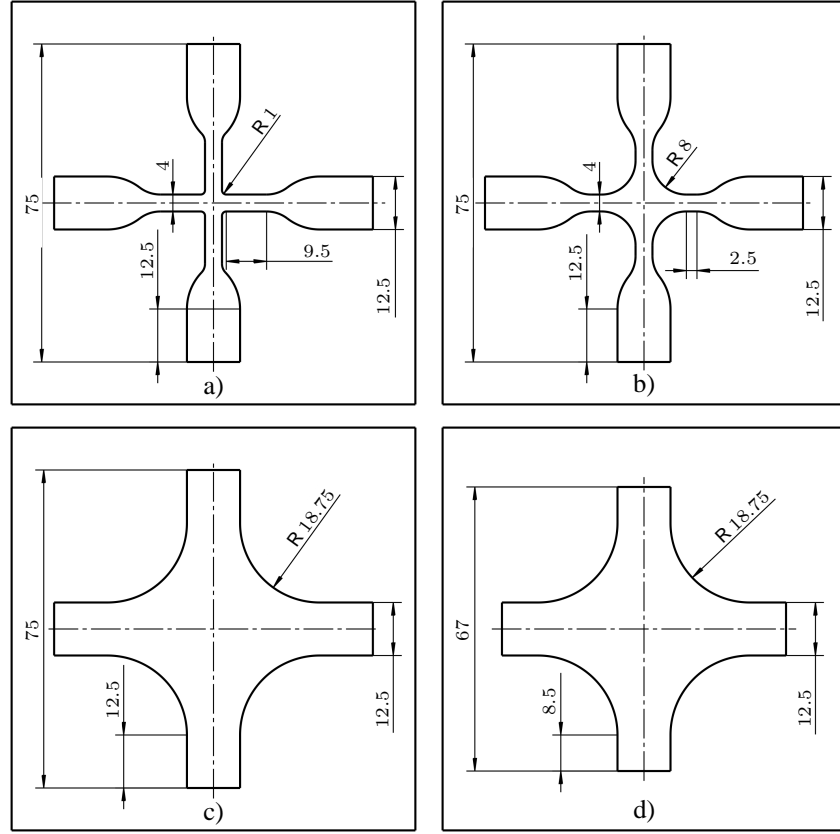
Figure 10: sample geometries: a) type A; b) type B; c) type C; d) type D

Fig. 3 and the one of the software Vic2D® is presumed. Furthermore it is assumed that these axes are principal axes of the strain tensor.

The principal strains in $x$- and $y$-direction can be extracted from the Green-Lagrangian strain tensor $\mathbf{E}$. In the following paragraphs they are described by the coefficients $E_{xx}$ and $E_{yy}$. Their pathway is carried out directly from the DIC-software.

For the case of a perfectly equibiaxial state in the centre of the specimen, marked by index $(\cdot)^c$, one has

$$E_{xx}^c \equiv E_{yy}^c. \tag{5}$$

Mathematically this can be evaluated by calculating the difference between both values. The error which occurs between these strains is interpreted as a criterion for the distance to that perfect state of equibiaxiality. The test function $\Gamma(x, y)$ can be defined as

$$\Gamma(x, y) = |E_{xx}(x, y) - E_{yy}(x, y)|. \tag{6}$$

Pointwise evaluation of the test function over the horizontal axis Ⓐ - Ⓑ as shown in Fig. 11b), which corresponds to the $x$-axis, provides a parabolic graph as displayed in Fig. 11a). The parabolic shape ensues of the fact that the aberrations between the strains in the arms are quite high, due to a nearly uniaxial deformation state in the arms. Ideally, the value of the test function in the centre is identical to zero in the case of perfect equibiaxiality. Hence, small values of $\Gamma(x, y)$ are equivalent to small aberrations of the equibiaxial state, large values indicate a nearly uniaxial state. With intent to achieve a geometry with a maximum area of equibiaxial deformation, the resulting parabolas in Fig. 11a) have to exhibit a maximum stretch factor, in detail this is equal to a wide graph. The minimum of the curves is by the construction located at the centre of the specimen.

A mathematical approach to benchmark the width of the plots is to calculate the standard deviation of $\Gamma(x, y)$ around the mean value, evaluated in a specified set of pixels around the angular point. Therefore, an acquisition area of 11 pixels is chosen, which is in accordance to the smallest area, Vic2D® is able to calculate the mean value over at the given arrangement.

Hence, a small standard deviation $\sigma_\Gamma^c$ over the observed field is synonymous with small aberrations of the equibiaxial state in it. Specimens with large (equi-)biaxial areas are obliged to show small standard deviations around the mean value of $\Gamma(x, y)$ in a specified range. By examination of Table 2 it is obvious that the shape D performs best in this test. The measured standard deviations of type A and type B are higher about one order.
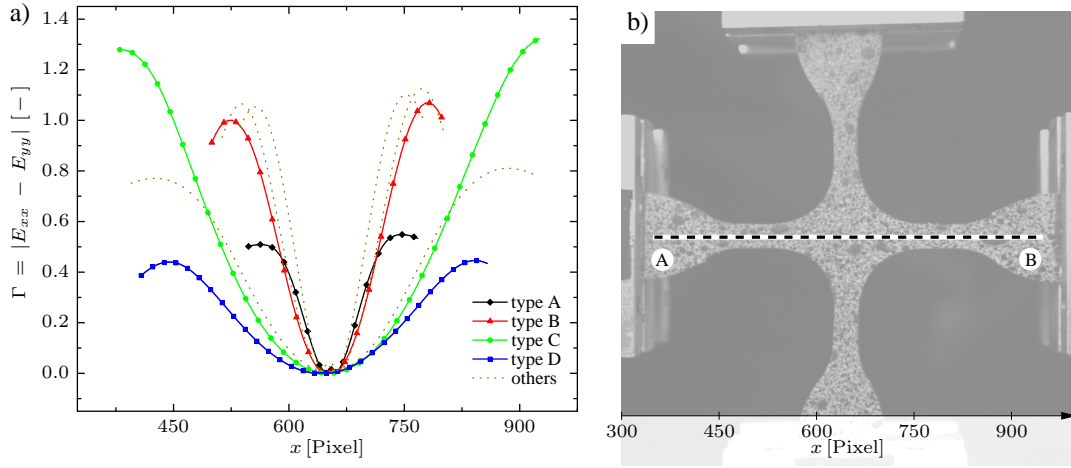
Figure 11: test function $\Gamma$ over horizontal symmetry axis Ⓐ - Ⓑ

Table 2: resulting values of the different specimens

| Sample | standard deviation $\sigma_\Gamma^c$ | scaled degree of efficiency $\eta^{(0.1)}$ | quality factor $Q^{(0.1)}$ |
|--------|------|------|------|
| type A | 0.05984 | 0.253 | 0.04 |
| type B | 0.05158 | 0.124 | 0.02 |
| type C | 0.00705 | 0.092 | 0.13 |
| type D | 0.00289 | 0.299 | 1.03 |

### 4.2.2 Degree of Efficiency (DOE)

The obtained results are not sufficient to make a statement about the qualification of the geometry. The basis for the evaluated curves in Fig. 11 are states which show a strain $E_{xx}^c \approx 0.1$ in the specimen's centre field. Besides the achievement above, a comparison between the strains in the arms of the particular samples shows high disparities. The strains occurring in the uniaxial regions are much higher than those in the biaxial regions. On this account, further investigations have to be carried out. At this point, the definition of a degree of efficiency (DOE) is inevitable to get more information. Obviously some geometries of the samples seem to promote a high gradient between the strain in the arms and in the crossroad area, respectively, which is in fact the scope of interest. High strains in the arms compared with that in the middle of the specimen imply high demands to the sample material. The required formulation of a degree of efficiency has to accommodate the proportionality between their respective strains. Therefore, the ratio has to depend on the strain in the crossroad area and also on the maximum strain in the specimen. It can be defined by

$$\eta = \frac{E_{xx}^c}{E_{xx}^{max}}.$$

Because of symmetry, it is adequate to evaluate the degree of efficiency in one direction, in this case the $x$-direction. In order to create comparability, the deformations with a centre field strain of $E_{xx}^c \approx 0.1$ are considered. Therewith, the scaled degree of efficiency can be written as

$$\eta^{(0.1)} = \frac{0.1}{E_{xx}^{max}}, \qquad \text{with } E_{xx}^c = 0.1. \tag{7}$$

Analysis of the scaled degree of efficiency in Table 2 bares the inadequacy of the sample of type C. The strains in the arms, which are necessary to create a centre field strain of 10 percent, are disproportionally high, even though the biaxially deformed field is large and therewith, the resulting standard deviation of $\Gamma(x, y)$ is small. The degree of efficiency is the main reason for varying the sample's geometry with respect to that proposed in Kahraman and Haberstroh (2013). In order to generate a large homogeneity in the specimen's centre there are multiple slits in the arms of the sample which yield a small degree of efficiency and therewith high demands on the sample. Depending on the extensibility of the material this can lead to limitations in the experimental investigations.
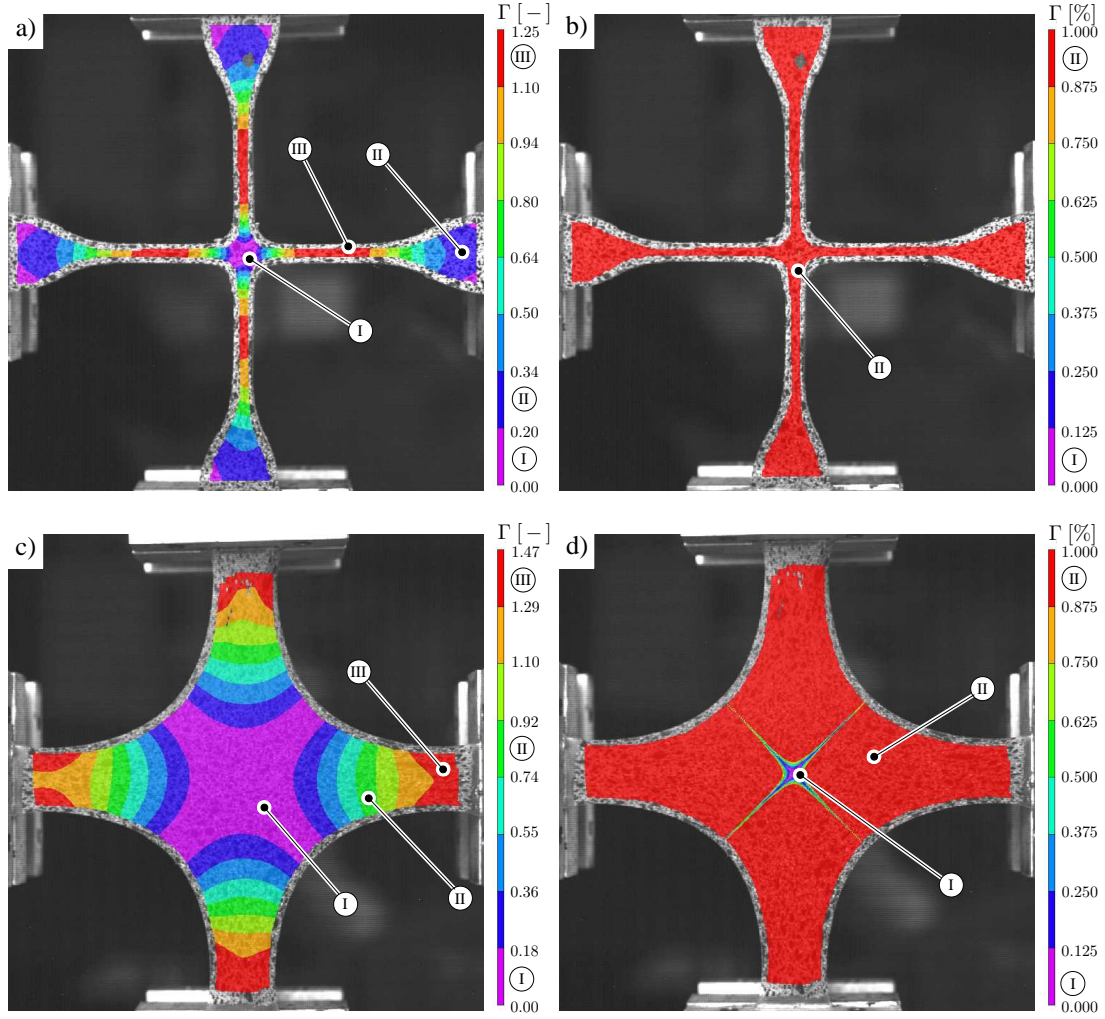
84

Figure 12: test function $\Gamma(x, y)$ on type A (top) and type D (bottom); left: auto-scaled, right: max. value $1\%$

A significant criterion for the suitability of the specimen has to adhere both factors. With this knowledge, it is possible to define a quality criterion $Q^{(0.1)}$ like

$$Q^{(0.1)} = \frac{\eta^{(0.1)}}{100 \cdot \sigma_\Gamma^c}. \tag{8}$$

Comparing the values for $Q^{(0.1)}$ in Table 2 carries out considerable differences between the particular sample geometries. Relating to the degree of efficiency $\eta^{(0.1)}$, type A represents a quite useful alternative to type D. The main disadvantage of this geometry is rooted in the bad standard deviation $\sigma_\Gamma^c$. Fig. 12 illustrates a comparison between those two samples. Both upper images show the original geometry (type A) as used in Johlitz and Diebels (2011), the lower ones show the ascertained type D. For a detailed view on the colour scheme the reader is referred to the online version of this paper. Therein the scale of the left images is adapted to the globally appearing values, the maximum value on the right images is set to a fix scale of one percent. That means, only the area with smaller aberrations of the equibiaxial state than one percent is coloured different than red (region ⓘⓘ in Fig. 12b) and d). In Fig. 12b) of type A such a district is only detectable by applying a zoom function so the whole surface shows larger deviations of the equibiaxial state. In Fig. 12d) this field is nearly as big as the crossroad area of the original shape (region ⓘ in Fig. 12d).

## 4.3 Evaluation of the Results

In order to verify the obtained results, this paragraph is intended to present a simple method to evaluate the foregoing considerations. In the case of admissibility of the developed criteria, the coupling between both axes has to depend characteristically on the particular geometry. With regard to illustrate this fact, it is possible to check
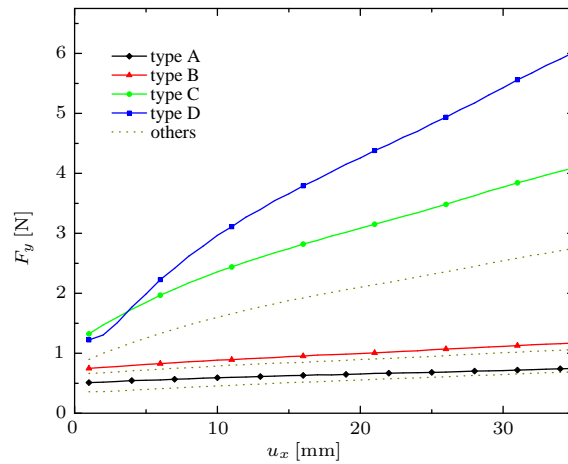
Figure 13: Evaluation: reaction force $F_y$ over distance covered by the linear slides $u_x$

the impact of deformation of the $x$-axis on the corresponding reaction force in the $y$-direction. By the creation of large biaxially deformed areas and small losses of strain in the arms, the influence of the lateral contraction in the crossroad area is maximised. Furthermore, the samples with slight strains outside the centre fields display a higher global stiffness than those with large strains outside that field.

The experiment, which is intended to prove this, is the simplest possible. Deforming the samples in one axis and observing the reaction force in the other one can support the assertion above. Fig. 13 shows the measurements following the mentioned test. One can see an explicit dependency of the reaction force in cross direction on the used sample geometry. Comparing the plots in terms of the quality factor $Q^{(0.1)}$ according to Table 2 it gets clearly evident that both statements coincide. The larger the value of the quality factor, the larger the slope of the reaction force induced by a deformation in the perpendicular direction.

As a result one can note the use of the generated quality criterion on the one hand, and also the suitability of the sample, that is optimised with that criterion. Hence it is not necessary to produce the geometry with the aid of complex manufacturing techniques. It can be cut out of a membrane. Consequentially, the material behaviour of the specimen is representative for the material which is used in the real application by the absence of specific molding processes or similar methods. Furthermore the requirements to the material concerning the uniaxial stretch are quite weak, which had been a basic demand.

## 5  Conclusion

The foregoing article introduces an in-house device to determine material parameters of elastomers under biaxial deformation. Therein the necessity of enquiring the influence of multiaxiality is illustrated by a typical component out of automotive engineering as an example. Combined with the results in Johlitz and Diebels (2011) one can recognize the importance of extending the experimental portfolio about a biaxial tension test. In this context, the course of a possible method of analysing the tests is mentioned. Therefore, the basic concepts of the inverse calculation in a simulation tool like Comsol Multiphysics® are presented.

For the optimisation of the constitutive parameters, the output of the simulation is compared to the experimentally obtained deformations.

In order to widen the biaxially deformed area in the specimen's centre, an enhanced sample geometry is introduced by defining a mathematically traceable quality criterion by the use of optical field measurement of the strain. The developed geometry fulfils the conditions regarding to producibility and the finite capability of resistance of the tested materials.

The influence of the biaxial deformation with respect to viscoelastic material behaviour is not investigated at this point.

## 6 Outlook

The experimental setup introduced in this work deals with nearly hyperelastic material on the one hand and a quasi static experimental arrangement on the other. Earlier works of Sedlan (2001), Koprowski-Theiß et al. (2011) or Scheffer et al. (2013) already describe the influence of a suitable pretreatment of viscoelastic specimens concerning the duration of experiments using uniaxial tension tests. In the future, the investigations about (cyclic) multiaxial deformations on viscoelastic materials have to be executed. For determining the hyperelastic and viscoelastic part of a resulting material model, the basic elasticity of the material has to be measured. Scheffer et al. (2013) propose a method to optimise the experimental duration for the case of uniaxial deformation. Following works will deal with the examination of the transfer of this method to biaxial deformations, which seems to be useful considering the interpretation of the pilot survey. The experimental effort to generate a data pool can be reduced by such a method.

Detailed investigations assume the reconstruction of the biaxial testing device with the goal of dynamic experiments. After that, systematic studies of viscous effects will be executed and interpreted.

Besides this constructive improvement of the device, a further numerical simulative optimisation of the sample geometry by using the ascertained knowledge of the experimental optimisation will follow.

## References

Avril, S.; Bonnet, M.; Bretelle, A.-S.; Grédiac, M.; Hild, F.; Ienny, P.; Latourte, F.; Lemosse, D.; Pagano, S.; Pagnacco, E.; et al.: Overview of identification methods of mechanical parameters based on full-field measurements. *Experimental Mechanics*, 48, 4, (2008), 381–402.

Baaser, H.; Hopmann, C.; Schobel, A.: Reformulation of strain invariants at incompressibility. *Arch Appl. Mech.*, pages 1–8.

Baaser, H.; Noll, R.: Simulation von Elastomerbauteilen - Materialmodelle und Versuche zur Parameterbestimmung. In: *DVM-Tag 2009* (2009).

Baaser, H.; Schobel, A.; Michaeli, W.; Masberg, U.: Vergleich von äquibiaxialen Prüfständen zur Kalibrierung von Werkstoffmodellen. *KGK Kautschuk Gummi Kunststoffe*, 5, (2011), 20.

Brown, R.: *Physical Testing of Rubber*. Springer-Verlag (2006).

Chatraei, S.; Macosko, C. W.: Lubricated squeezing flow: a new biaxial extensional rheometer. *Journal of Rheology*, 25, (1981), 433.

Chen, Z.; Scheffer, T.; Seibert, H.; Diebels, S.: Macroindentation of a soft polymer: Identification of hyperelasticity and validation by uni/biaxial tensile tests. *Mech. Mater.*, 64, 0, (2013), 111 – 127.

Chevalier, L.; Marco, Y.: Tools for multiaxial validation of behavior laws chosen for modeling hyper-elasticity of rubber-like materials. *Polym. Eng. Sci.*, 42, 2, (2002), 280–298.

Chu, T.; Ranson, W.; Sutton, M.: Applications of digital-image-correlation techniques to experimental mechanics. *Exp. Mech.*, 25, 3, (1985), 232–244.

Correlated Solutions: *Vic2D Manual* (2010).

De Crevoisier, J.; Besnard, G.; Merckel, Y.; Zhang, H.; Vion-Loisel, F.; Caillard, J.; Berghezan, D.; Creton, C.; Diani, J.; Brieu, M.; Hild, F.; Roux, S.: Volume changes in a filled elastomer studied via digital image correlation. *Polym. Test.*, 31, 5, (2012), 663–670.

Demmerle, S.; Boehler, J.: Optimal design of biaxial tensile cruciform specimens. *J. Mech. Phys. Solids*, 41, 1, (1993), 143–181.

Detrois, C.: *Untersuchungen zur Dehnrheologie und Verarbeitbarkeit von Halbzeugen beim Thermoformen sowie Simulation und Optimierung der Umformphase*. Ph.D. thesis, RWTH Aachen (2001).

Eyerer, P.; Hirth, T.; Elsner, P.: *Polymer Engineering*. Eyerer, P. (2008).

Freund, M.; Lorenz, H.; Juhre, D.; Ihlemann, J.; Klüppel, M.: Finite element implementation of a microstructure-based model for filled elastomers. *Int. J. Plast.*, 27, 6, (2011), 902–919.

Gent, A.: Simple rotary dynamic testing machine. *British Journal of Applied Physics*, 11, 4, (1960), 165.

Gent, A.: *Engineering with rubber: How to design rubber components*. Hanser Gardner Publications (2001).

Haupt, P.; Lion, A.: On finite linear viscoelasticity of incompressible isotropic materials. *Acta Mech.*, 159, 1, (2002), 87–124.

Ihlemann, J.: *Kontinuumsmechanische Nachbildung hochbelasteter technischer Gummiwerkstoffe*. 18, VDI-Verlag, 288 edn. (2002).

Johlitz, M.; Diebels, S.: Characterisation of a polymer using biaxial tension tests. part I: Hyperelasticity. *Arch Appl. Mech.*, 81, 10, (2011), 1333–1349.

Kahraman, H.; Haberstroh, E.: Direction-dependent and multiaxial stress-softening behavior of carbon black-filled rubber. *Rubber Chemistry and Technology*.

Klauke, R.; Alshuth, T.; Ihlemann, J.: Lifetime prediction of rubber materials under simple shear load with rotating axes [lebensdauervorhersage von technischen gummiwerkstoffen unter einfacher scherung mit rotierenden achsen]. *KGK Kautschuk Gummi Kunststoffe*, 63, 7-8, (2010), 286–290.

Koprowski-Theiß, N.; Johlitz, M.; Diebels, S.: Modelling of a cellular rubber with nonlinear viscosity functions. *Exp. Mech.*, 51, 5, (2011), 749–765.

Koprowski-Theiß, N.; Johlitz, M.; Diebels, S.: Pressure dependent properties of a compressible polymer. *Exp. Mech.*, 52, 3, (2012), 257–264.

Kuwabara, T.: Advances in experiments on metal sheets and tubes in support of constitutive modeling and forming simulations. *Int. J. Plast.*, 23, 3, (2007), 385–419.

Lion, A.: *Thermomechanik von Elastomeren: Experimente und Materialtheorie*. Inst. für Mechanik (2000).

Makinde, A.; Thibodeau, L.; Neale, K.: Development of an apparatus for biaxial testing using cruciform specimens. *Exp. Mech.*, 32, 2, (1992), 138–144.

Mooney, M.: A theory of large elastic deformation. *J. Appl. Phys.*, 11, 9, (1940), 582–592.

Ohtake, Y.; Rokugawa, S.; Masumoto, H.: Geometry determination of cruciform-type specimen and biaxial tensile test of c/c composites. *Key Engineering Materials*, 164, (1998), 151–154.

Pan, B.; Qian, K.; Xie, H.; Asundi, A.: Two-dimensional digital image correlation for in-plane displacement and strain measurement: A review. *Meas. Sci. Technol.*, 20, 6, (2009), 062001.

Payne, A.: The dynamic properties of carbon black-loaded natural rubber vulcanizates. part I. *J. Appl. Polym. Sci.*, 6, 19, (1962), 57–63.

Promma, N.; Raka, B.; Grédiac, M.; Toussaint, E.; Le Cam, J.; Balandraud, X.; Hild, F.: Application of the virtual fields method to mechanical characterization of elastomeric materials. *Int. J. Solids Struct.*, 46, 3, (2009), 698–715.

Reese, S.; Govindjee, S.: A theory of finite viscoelasticity and numerical aspects. *Int. J. Solids Struct.*, 35, 26, (1998), 3455–3482.

Rey, T.; Chagnon, G.; Le Cam, J.; Favier, D.: Influence of the temperature on the mechanical behaviour of filled and unfilled silicone rubbers. *Polym. Test.*, 32, 3, (2013), 492–501.

Rivlin, R.; Saunders, D.: Large elastic deformations of isotropic materials. VII. Experiments on the deformation of rubber. *Philosophical Transactions of the Royal Society of London. Series A, Mathematical and Physical Sciences*, 243, 865, (1951), 251–288.

Sasso, M.; Palmieri, G.; Chiappini, G.; Amodio, D.: Characterization of hyperelastic rubber-like materials by biaxial and uniaxial stretching tests based on optical methods. *Polym. Test.*, 27, 8, (2008), 995–1004.

Scheffer, T.; Seibert, H.; Diebels, S.: Optimisation of a pretreatment method to reach the basic elasticity of filled rubber materials. *Arch Appl. Mech.*, accepted.

Schmidt, T.; Tyson, J.; Galanulis, K.: Full-field dynamic displacement and strain measurement using advanced 3D image correlation photogrammetry: Part 1. *Experimental Techniques*, 27, 3, (2003a), 47–50.

Schmidt, T.; Tyson, J.; Galanulis, K.: Full-field dynamic displacement and strain measurement using advanced 3D image correlation photogrammetry: Part 2. *Experimental Techniques*, 27, 4, (2003b), 22–26.

Sedlan, K.: *Viskoelastisches Materialverhalten von Elastomerwerkstoffen: Experimentelle Untersuchung und Modellbildung*. Berichte des Institut für Mechanik 2/2001, Universität Kassel (2001).

Silberstein, M.; Pillai, P.; Boyce, M.: Biaxial elastic-viscoplastic behavior of nafion membranes. *Polym.*, 52, 2, (2011), 529–539.

Sutton, M.; McNeill, S.; Helm, J.; Chao, Y.: *Advances in two-dimensional and three-dimensional computer vision*. Springer (2000).

Sutton, M.; Orteu, J.; Schreier, H.: *Image correlation for shape, motion and deformation measurements: Basic Concepts, Theory and Applications*. Springer (2009).

Tiernan, P.; Hannon, A.: Design optimisation of biaxial tensile test specimen using finite element analysis. *Int. J. Mater. Form.*, 0, 1, (2012), 1–7.

Treloar, L.: *The physics of rubber elasticity, 3rd edn. Clarendon*. Oxford (1975).

Treloar, L.: Mechanics of rubber elasticity. *Proc R Soc London Ser A*, 351, 1666, (1976), 301–330.

Yaofeng, S.; Pang, J.: Study of optimal subset size in digital image correlation of speckle pattern images. *Opt. Lasers Eng.*, 45, 9, (2007), 967–974.

---

*Address:* Dipl. Ing. Henning Seibert, Chair of Applied Mechanics, Saarland University, Campus, bldg. A 4.2, D-66123 Saarbrücken
email: `h.seibert@mx.uni-saarland.de`